Molecular Network Development and Evolution of Nanoscale Morphology in an Epoxy-Amine Thermoset Polymer

Christopher M. Sahagun, Katrina M. Knauer, Sarah E. Morgan

School of Polymers and High Performance Materials, University of Southern Mississippi, Hattiesburg, Mississippi 39401

Received 5 August 2011; accepted 4 January 2012
DOI 10.1002/app.36763
Published online in Wiley Online Library (wileyonlinelibrary.com).

ABSTRACT: Epoxy-amine thermoset polymers exhibit a complicated, highly crosslinked network structure. The connectivity of this network drives material parameters such as mechanical properties and solvent permeation. Understanding the molecular network architecture is also an important aspect of the developing realistic network topologies for use in molecular dynamic simulations. Here, the evolution of network connectivity in a typical crosslinked epoxy-amine network (Epon 828/3-aminophenyl sulfone) is monitored as a function of cure time. Special attention is paid to nanoscale variation in the crosslink density of the network. Submicron atomic force microscope images of sample fracture surfaces revealed three distinct types of crack tip propagation. Near-infrared spectroscopy, rheological and thermal characterization were used to correlate each type of fracture propagation behavior to a different stage of network development. Monitoring changes in the nanoscale fracture behavior reveals information regarding changes in the network architecture during cure and provides insight into the final structure of the epoxy-amine network. © 2012 Wiley Periodicals, Inc. J Appl Polym Sci 000: 000–000, 2012

Key words: epoxy resins; nanoscale morphology; thermoset network; sol–gel–glass transformation

INTRODUCTION

With the increased use of polymer matrix composites in replacement of traditional materials for aerospace, naval, energy, and construction applications, there is an increased need for understanding of the molecular level mechanisms that drive ultimate composite performance.[1] Advanced nanoprobe techniques, in combination with spectroscopic, rheological, thermal, and dynamic–mechanical analysis, provide a platform for determining structure at the molecular level in complex crosslinked systems and predicting composite performance, including water and solvent penetration, thermal and electrical conductivity, dielectric properties, mechanical properties, and fracture behavior.[2–10] Additionally, recent advancements in the ability to predict material behavior computationally have led to renewed interest in discerning the true network architecture of cured epoxy systems.[11–14] This work provides insight into the actual molecular-scale connectivity of the fully cured epoxy amine thermoset molecular networks. Understanding the true molecular scale connectivity will help ensure that computational experiments are conducted on realistic network topologies.

Thermosetting epoxy-amine systems are an important class of network polymers with favorable thermal properties, mechanical properties, and solvent resistance. These properties make epoxy-amine systems an attractive choice for the polymeric matrix of the high-performance composites found in aerospace, sports, and automotive applications. Epoxy-amine systems derive their physical properties from their complicated, highly crosslinked molecular network. Therefore, the true molecular structure of these networks must be understood to discern the molecular-scale root of these properties. Unfortunately, the intractable nature of the crosslinked network makes characterization of the network connectivity of these systems difficult. This work addresses questions regarding the submicron distribution of crosslink density within a typical epoxy-amine thermoset system by monitoring changes in nanoscale fracture behavior with respect to chemical conversion of the amine curing agent and also investigates key stages in the physical development of the crosslinked network. Understanding the network

Additional Supporting Information may be found in the online version of this article.

Correspondence to: S. E. Morgan (sarah.morgan@usm.edu).

Contract grant sponsor: Office of Naval Research; contract grant number: N00014-07-105.
Contract grant sponsor: NSF REU; contract grant number: 1005127.

structure will ensure that simulations are conducted on realistic network topologies and will also aid in the molecular scale understanding of pathway-dependent properties such as crack tip propagation and solvent penetration.

The crosslink density of the epoxy-amine network has a particularly strong influence on the physical properties of the system. Chemically similar epoxy-amine systems with different crosslink densities exhibit different physical and thermal properties as well as different fracture and solvent transport behavior.[15–18] Just as differences in bulk crosslink density lead to different bulk properties, it is reasonable to expect that localized differences in crosslink density will lead to local regions with different properties. The distribution of crosslinks within a network defines the molecular connectivity, or topology, of the system, and understanding this molecular connectivity is one of the most important aspects of predicting final part performance.[19] At the molecular scale, individual crosslinks within the network serve as barriers to solvent penetration and crack-tip propagation—the solvent molecule must travel around the crosslink and the propagating crack tip must either expend energy to break the covalent bond or find a path around it. These processes are energy dependent and a solvent molecule or propagating crack tip will preferentially deviate to follow the lowest-energy pathway through the network. Regions of the thermoset network with relatively lower degrees of crosslinking serve as these low-energy pathways. Pathway dependent properties such as solvent penetration and fracture propagation, therefore, can serve as indicators of network heterogeneity in epoxy-amine systems.

Epoxy-amine networks have long been suspected of possessing a nonhomogeneous distribution of crosslinks within the network structure. The nodular morphology observed in early scanning electron microscopy studies of cured epoxy-amine samples was put forth as some of the initial evidence of nonheterogeneity in the network structure of these systems.[20–23] These results were criticized, however, as the possibility that the observed morphology was merely an effect of etching by the electron beam.[24] The recent advent of atomic force microscopy has provided a means to interrogate nanoscale morphology that was free from the potential for etching-induced artifacts. Atomic force microscope (AFM) studies on fully cured epoxy-amine systems have revealed a nanoscale morphology very similar to that seen in SEM micrographs.[25–28] This nodular morphology has been reported under a variety of cure conditions and is found at both the fracture surface and at surfaces etched by ion and ultraviolet radiation. This indicates that the nodular nanostructures are a real component of the network and do not result from either a fault in processing or from the fracture process.

More direct evidence has also been cited as an indication of nonhomogeneous structure in epoxy-amine networks. An epoxy-amine system strained while being monitored in a scanning electron microscope was found to contain 6–9 nm particles that remained intact even as the surrounding material flowed in response to the strain.[29] The nodular nanostructures are especially clear at the fracture surface of samples and, as shown by this work, appear only after the gel point and become more distinct as cure progresses. This behavior indicates that these structures result from the underlying molecular network and that their presence influences the crack tip propagation pathway. Additional evidence for network heterogeneity has been reported from small angle neutron scattering studies of epoxy-amine systems swollen with deuterated solvent.[17,25,30] Like fracture propagation, solvent penetration is pathway dependent. These studies show that samples tend to preferentially swell in domains on the order of 40–60 nm. This is similar in size to the nanostructures observed microscopically. Additional evidence for a nonhomogeneous network structure has been cited from dynamic mechanical analysis, swelling behavior and small angle X-ray scattering.[31–33] This work provides further evidence as to the nonhomogeneity of cured epoxy-amine systems by monitoring the development of the nonhomogeneous network architecture through the early stages of cure up to the onset of vitrification.

Nonhomogeneity of the molecular structure has been shown to influence the path chosen by the propagating crack tip in other polymeric systems. Microscopic investigation of pressure-crystallized Nylon-6 fracture surfaces has shown that a crack will preferentially propagate along lamellar boundaries.[34] Additionally, microscopic investigation of the fracture surface of a spherulite-containing polypropylene has shown that the crack tip preferentially propagates through spherulitic boundaries.[35] The commonality between these two results is that the propagating crack tip was found to deviate in response to the underlying molecular structure. Specifically, the crack tip deviated to preferentially propagate through regions with a relatively lower number of strong covalent bonds. This deviation was preserved at the fracture surface of the material, allowing regions with relatively higher amounts of covalent bonding to be identified. In a similar way, this work utilizes nanoscale fracture behavior to identify the distribution of network heterogeneity in a typical epoxy-amine system. Chemical conversion of the amine curing agent is monitored by near-infrared (NIR) spectroscopy while key points in the physical development are identified rheometrically

and thermally. These changes are then utilized in the analysis of images obtained by atomic force microscopy to identify the underlying network structure of the epoxy-amine system at various points of the curing reaction.

EXPERIMENTAL

Materials

The diglycidyl ether of bisphenol A Epon 828 was purchased from E.V. Roberts Co. (Carson, CA). Epon 828 is a low-molecular weight difunctional epoxy oligomer that was received as a clear viscous liquid. 3,3′-Diaminodiphenyl sulfone (DDS) was purchased from Tokyo Chemical Industry Company. DDS is a tetrafunctional aromatic amine that was received as a fine white powder. The chemical structures of the epoxy component and the amine curing agent are shown in Figure 1. All materials were used as received.

Sample preparation

Resin mixing

Epon 828 was mixed with DDS in a 1 : 1 stoichiometric ratio based on monomer functionality. Around 20 g of Epon 828 were placed in a standard laboratory beaker and immersed in an oil bath at 130°C. The appropriate amount of DDS was added and the mixture was stirred mechanically at 130°C under normal atmospheric conditions. The addition of DDS was taken to be the zero-time ($t = 0$) for the curing reaction. Each batch was allowed to stir for 20 min at which point no DDS was visible in the beaker and the mixture was a clear, low viscosity liquid. The mixed resin was then immediately prepared for specific tests.

Fracture surface preparation

All AFM and nanoindentation testing was conducted on bulk material exposed by fracture. Samples for fracture were produced by pouring the mixed Epon 828/DDS resin into silicone molds that had been preheated to 130°C. Each mold was 1 cm × 6 cm × 0.5 cm giving a sample volume of 3 cm^3. These dimensions ensured that each sample was thick enough to produce a large core of bulk material while still being easy to fracture. The filled molds were returned to the oven and the curing reaction was allowed to proceed at 130°C under normal atmosphere and pressure for predetermined lengths of time to give a series of samples with increasing degrees of network development. The system had a T_g above room temperature after around 75 min of cure, meaning that samples were mechanically stable and could be fractured at room temperature after this point. Each sample was then cooled to 2°C to arrest the curing reaction. Samples were fractured by hand to expose bulk material immediately prior to testing.

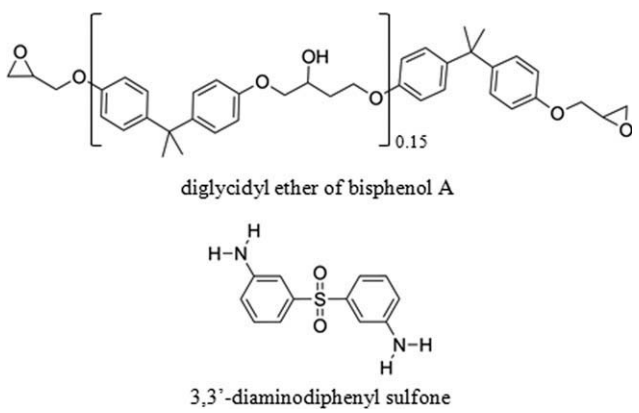

Figure 1 Chemical structure of Epon 828 and 3,3′-diaminodiphenyl sulfone.

Atomic force microscopy

The evolution of the fracture surface morphology was monitored with a Dimension 3000 AFM from Veeco Instruments (Santa Barbara, CA) equipped with an optical positioning system. Surface topography images of the fracture surface at increasing levels of cure were made with a silicon probe with a 125-μm long cantilever and a nominal spring constant of 40 N/m operated in tapping mode at its resonance frequency of around 370 kHz. The tip had a nominal radius of curvature of 8 nm. The cantilever's tapping amplitude during imaging was maintained at around 85–90% of the free amplitude to minimize cantilever-induced surface deformation while also allowing adequate tracking of the sample surface. AFM imaging was conducted under ambient conditions in a temperature (20°C) and humidity (40–45%) controlled room.

Samples were affixed to an AFM stage puck with putty. The optical positioning system was used to find a suitably flat region to image. Images were preferentially taken at the "mirror" region of the fracture surface. However, the mirror region was inaccessible for some samples so images were instead made on the "mist" region of fracture. Initial studies showed that identical nanoscale morphologies were seen on the mirror, mist, and hackle regions of the fracture surface, providing further evidence that these structures result from the network architecture, not the fracture process.

A total of 750 nm × 750 nm area was scanned at a rate of 0.75 Hz with a resolution of 512 × 512 pixels. Multiple areas were scanned for each sample and figures presented here show representative morphology. Images and statistical quantities were processed with Gwyddion v.2.24 SPM analysis software. Image processing was limited to data leveling by

plane subtraction and the correction of scan line artifacts. Root mean square (RMS) roughness for each sample was calculated according to ASME B46.1-1995.[36] RMS roughness describes the height deviation of individual data points (pixels) measured from the mean surface-height plane and is given by the following equation:

$$R_{\mathrm{RMS}} = \sqrt{\frac{1}{N}\sum_{j=1}^{N} r_j^2} \quad (1)$$

where N is the total number of pixels and r_j is the vertical distance of pixel j from the mean surface-height plane.

Rheometry

The evolution of the dynamic shear moduli during the curing reaction was monitored with an ARES Rheometer from TA Instruments (New Castle, DE) equipped with a heating oven. After mixing, the liquid Epon 828/DDS mixture was poured directly onto 25 mm aluminum parallel plates that had been preheated to 130°C. Care was taken to avoid the introduction of air bubbles and any resin overflow was removed from the edges of the sample holder. Testing was conducted with a gap of 1 mm. The ARES rheometer is capable of MultiWave testing which allows multiple frequencies to be tested simultaneously over two orders of magnitude.[37] This is advantageous as it reduces the amount of time required for measurement. Each test took around 25 s, meaning that cure progressed to some degree during the time required to complete the measurement; however, this time is small compared with the overall time the sample was monitored. Thus any change in the network from the beginning to the end of each individual test is small enough not to affect the measurement to a large degree. The storage (G') and loss (G'') moduli were measured every 2 min at frequencies of 0.5, 1, and 50 rad/s, simultaneously. These values were used to calculate the loss tangent (tan δ):

$$\tan\ \delta = \frac{G''}{G'} \quad (2)$$

The gel point was identified as the time at which the value of tan δ is independent of frequency.[38,39] Each measurement was made at 0.1% strain as this was sufficiently low to avoid non-newtonian effects and network breakdown. Initial tests were conducted to ensure all measurements were made in the linear viscoelastic region.

Differential scanning calorimetry

A Q100 differential scanning calorimeter (DSC) from TA Instruments (New Castle, DE) was used to monitor the evolution of the glass transition temperature with cure time. Approximately 12 mg of the mixed resin was placed into hermetically sealed aluminum DSC pans. Samples were held at 130°C in the DSC for predetermined lengths of time and then thermally scanned from −10°C to 200°C at 20°C per minute. Data were analyzed with TA Universal Analysis v.4.5A. The T_g was taken as the inflection point of the exotherm.

Near-infrared spectroscopy

Monomer conversion was monitored by transmission NIR. A Nicolet 6700 spectrometer from Thermo Scientific (Waltham, MA) was used to monitor changes in transmission infrared (IR) absorption in the region 10,000–4000 cm^{-1} of samples with incrementally higher degrees of cure. Thirty-two scans were made of each sample with a resolution of 2 cm^{-1}.

Samples were made by first gluing 13 mm diameter, 0.75-mm thick PTFE washers to 25 mm diameter borosilicate glass microscope slide covers with a cyanoacrylate-based glue to ensure reasonably constant 0.75-mm path length in all samples. Care was taken to prevent contamination of the glass by vapors released as the glue cured. The sample holders were conditioned in a standard laboratory oven at 130°C overnight to help drive off any residual volatiles. The sample holders were then filled with the Epon 828/DDS mixture and capped with another slide cover. The prepared samples were placed in a standard laboratory oven at 130°C and allowed to cure for predetermined lengths of time. Samples were then removed from the oven and NIR spectra were obtained immediately after each sample reached room temperature.

Spectral analysis was performed with Essential FTIR v2.00.040 from Operant, LLC. The concentration of primary, secondary, and tertiary amine at increasing degrees of cure was calculated according to Beer's law in a similar way as the method reported by Min.[40] The absorbance of each component was found by integrating the peaks within the absorption bands listed in Table I. The difficulty of preparing sample with identical path lengths was overcome by using the phenyl group band at 4610–4690 cm^{-1} as an internal standard to normalize the integrated peak areas. As volume concentration is difficult to measure in the Epon 828/DDS mixture, the initial molar concentration (expressed as mol kg^{-1}) of each component of interest was used to calculate molar absorptivity. The absorption coefficient is frequency-specific and was therefore calculated for each component at the frequency range listed in Table I. The absorption coefficients of the primary amine and epoxy group were calculated from neat

TABLE I
Absorption Bands and Calculated Molar Absorptivities Used to Determine Concentration

Chemical group	Absorption band (cm^{-1})	Molar absorptivity (kg mol^{-1})
Phenyl	4610–4689	5.4
Epoxide	4520–4540	4.4
1° Amine	4520–4540	1.3
1° Amine	5040–5110	8.7
1° Amine	6610–6750	4.9
2° Amine	6610–6750	5.0

samples of their respective monomer. The molar absorptivity of the secondary amine was calculated by measuring the conversion of primary amine during the first 20 min of cure. It was assumed that the only reaction during this time was the conversion of primary amine to secondary amine and no secondary amine was converted to tertiary amine. This assumption is reasonable because of the higher reactivity of a primary aromatic amine compared with a secondary aromatic amine.[41] The concentration of secondary amine at $t = 20$ min can therefore be deduced by measuring the reduction of primary amine concentration during the first 20 min of cure. The molar absorptivity of the secondary amine was then calculated from its absorbance at 6610–6750 cm^{-1}.

The total absorbance from overlapping bands is the sum of the absorbances of the individual components. This allows for the deconvolution of the epoxide and primary amine absorption band at 4520–4540 cm^{-1}:

$$A_t = \varepsilon_{EP}[EP]_t + \varepsilon_{PA}[PA]_t \quad (3)$$

where A_t is the total band area at time t, ε_{EP}, and ε_{PA} are the molar absorptivities of the epoxy and primary amines, respectively, and $[PA]_t$ is the concentration of primary amine at time t calculated from the absorption band at 5040–5110 cm^{-1}. This equation was solved for $[EP]_t$ to find the concentration of epoxides at increasing lengths of cure time. The concentration of secondary amine can be similarly calculated from its convoluted absorption band at 6610–6750 cm^{-1}. The tertiary amine concentration is calculated from the balance of primary and secondary amine consumed and produced:

$$[TA]_t = [PA]_0 - [PA]_t - [SA]_t \quad (4)$$

where $[TA]_t$ is the concentration of tertiary amine at time t, $[PA]_0$ is the initial molar concentration of primary amine, and $[SA]_t$ is the concentration of the primary and secondary amine at time t, respectively.

Nanoindentation

Nanoindentation-based creep testing was performed with a TI 900 TriboIndenter from Hysitron (Minneapolis, MN). Samples were affixed to AFM stage pucks with a stiff epoxy putty. A load-controlled loading function consisting of a 100 μN/s loading segment, 60 s hold time at a peak load of 250 μN, and a 25 μN/s unloading segment was used for all tests. This force produced an indentation depth on a size scale similar to that of individual nodules. Three different fracture surfaces of each sample from a specific cure time were investigated. Ten indentations were made on each fracture surface for a total of 30 indentations per cure increment. Creep behavior was determined by monitoring indenter displacement as a function of load hold time. The Oliver–Pharr model was used for data analysis.[42]

RESULTS AND DISCUSSION

Characterization of network development

Network development consists of three distinct stages: pregelation, active network growth, and postvitrification. During the pregelation stage, there is no infinite molecular weight network. The gel point of the system marks the end of the pregelation stage and the beginning of the active network growth stage. During the active network growth stage, the sample consists of an infinite molecular weight "skeleton network" to which unreacted monomer and low-molecular weight oligomer is added. The majority of network growth occurs during this stage as unreacted species can easily diffuse to active reaction sites. The main stage of active network growth ends at the onset of vitrification. The final stage of network development is the postvitrification stage. During this stage, the network has grown sufficiently to restrict diffusion of unreacted species and the curing reaction becomes diffusion controlled. Rheometric and thermal testing was performed on the Epon 828/DDS system to identify the gel point and onset of vitrification, respectively, and thereby establish the boundaries of the three phases of network development.

Figure 2 shows the loss tangent of the Epon 828/DDS system measured at three different frequencies plotted as a function of cure time. The gel point is indicated by the point where the measured value of tan δ becomes frequency independent.[38,39] This occurs at the crossover point of the three frequency curves observed at 104 min of cure. Figure 3 shows T_g measured by DSC plotted as a function of cure time. Step-growth thermosetting polymers begin to vitrify as the T_g of the material approaches the reaction temperature.[43–45] In Figure 3, a change in slope

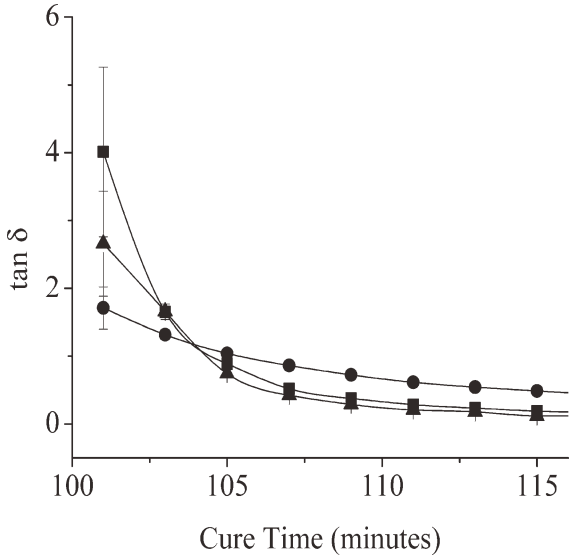

Figure 2 Tan δ as a function of cure time measured at 0.5 (■), 1 (•), and 50 rad/s (▲). The measured value of tan δ is independent of frequency at 104 min of cure time.

is observed at 210 min of cure time near the cure temperature of 130°C. This point was taken to mark the onset of vitrification.

Rheometric and thermal testing therefore establishes the boundaries of each of the three phases of network growth. Samples cured for <104 min are in the initial, pregel phase of growth and have yet to develop an infinite molecular weight network. These samples consist of low-molecular weight oligomer and unreacted monomer. Samples cured for >104 min (gel point) but fewer than 210 min (onset of vitrification) are in the active network growth stage. Samples at this stage possess an infinite molecular weight network and unreacted species are actively being added to the growing network. Samples cured for longer than 210 min are in the vitrification stage. These samples have a crosslink density high enough to restrict the diffusion of unreacted species to active reaction sites.

The influence of network development on nanoscale fracture propagation behavior

Each of the three stages of network development yields a different fracture surface morphology. These morphologies are shown in the topographic and AFM phase images presented in Figure 4. Figure 4(A), obtained from a sample in the initial pregelation stage of cure, shows the featureless, planar fracture surface typical of samples with low levels of network development. Figure 4(B–D), obtained from samples in the main stage of active network growth, exhibits the nodular nanostructures typical of epoxy-amine systems. These nanostructures are first observed in samples taken at the gel point [Fig. 4(B)] and appear more regular in samples taken near the onset of vitrification [Fig. 4(D), sample taken 20 min prior to the onset of vitrification]. Figure 4(E), obtained from a sample taken shortly after the onset of vitrification, shows a change in the fracture surface morphology, as the nodular nanostructures appear less defined and the surface is much rougher (Fig. 9).

AFM phase imaging provides information about the distribution of mechanical and viscoelastic properties of the network near the fracture surface by monitoring the way in which the oscillating tip interacts with the sample. This interaction, however, is also influenced by variation in the tip/sample contact area during scanning which affects the total amount of force applied to the surface by the oscillating tip.[46,47] This variation can cause non-network effects such as edges and sharp surface gradients to disproportionately affect the tip/sample interaction. The phase images in Figure 4 show that variation in the measured phase lag is concentrated in the region between nanostructures where the slope of the surface topography changes sharply.

Molecular structure development

Each amine moiety on the DDS monomer participates in two distinct reactions during cure. The primary amine will first react with an epoxide to produce a secondary amine which in turn reacts to form a tertiary amine. The reaction of the primary amine results in a linear segment while the secondary amine reaction produces either a branch or a crosslink. Using NIR spectroscopy, it is possible to discriminate between primary and secondary amines and thus gain understanding of the molecular structure of the developing network as a function of cure

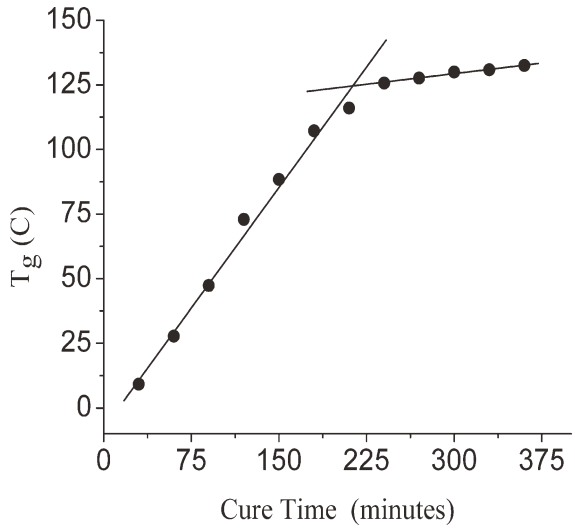

Figure 3 T_g as a function of cure time. The onset of vitrification occurs after 210 min of cure time.

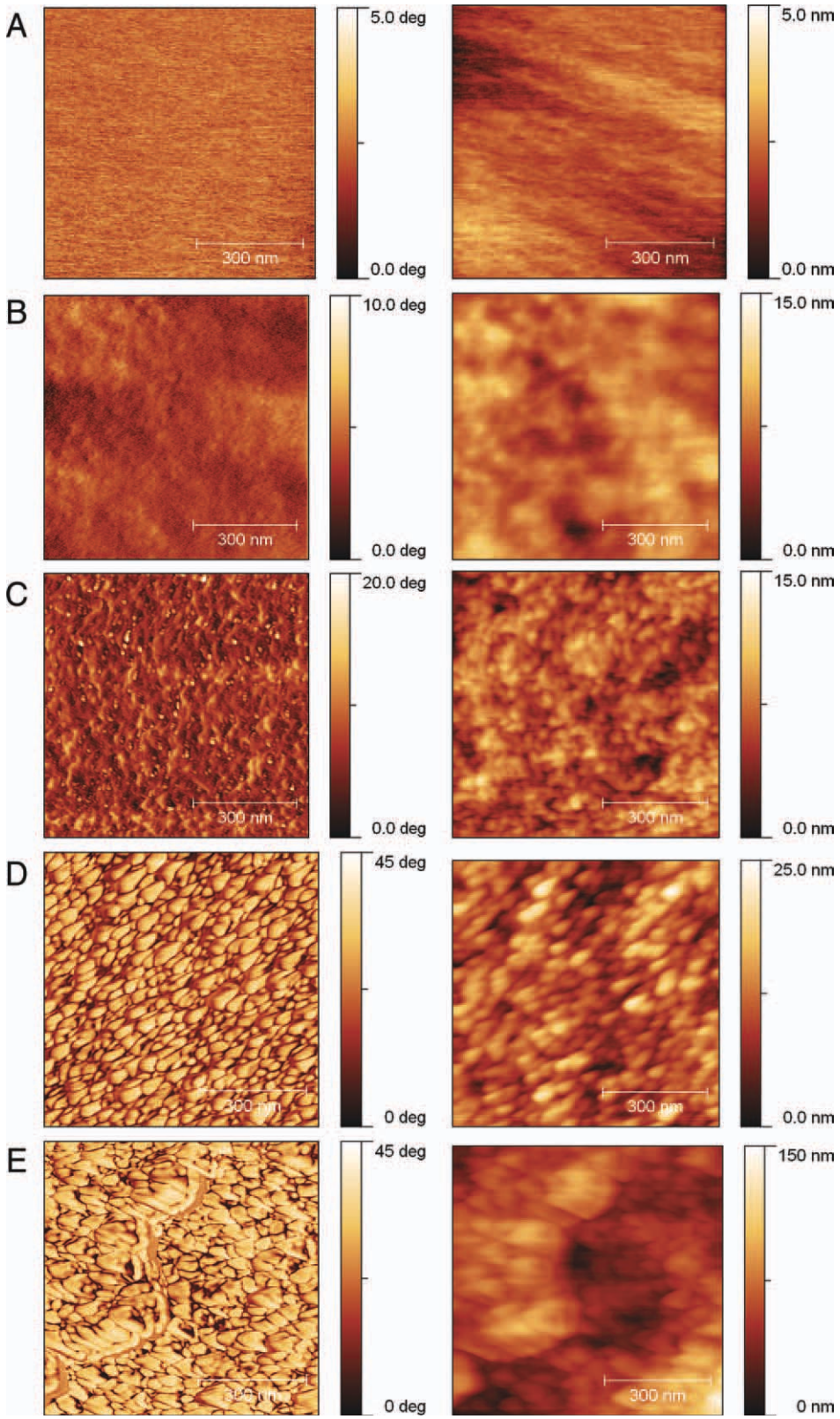

Figure 4 AFM topographic (left) and phase (right) images of the fracture surface of the epoxy-amine system at various stages of cure. Each image represents an area 750 nm × 750 nm. (A) 84 min (pregelation), (B) 104 min (gel point), (C) 124 min (active growth stage), (D) 184 min (active growth stage), and (E) 224 min (postvitrification). Each image is 750 nm × 750 nm. [Color figure can be viewed in the online issue, which is available at wileyonlinelibrary.com.]

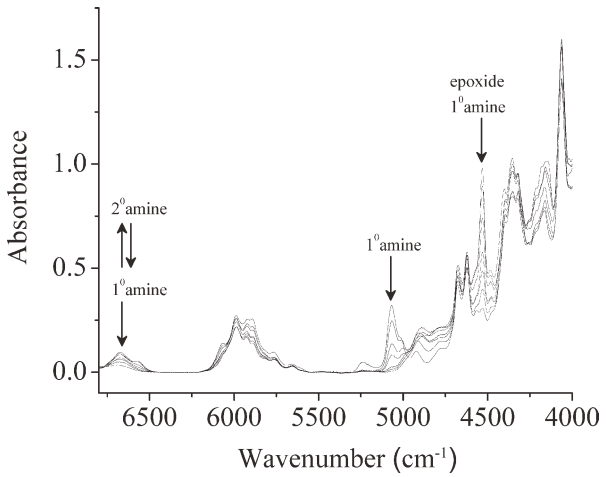

Figure 5 Near-infrared spectra of stoichiometric Epon 828/DDS mixtures at 0, 50, 94, 104, 144, and 234 min of cure showing epoxy conversion (4540–4550 cm^{-1}), primary amine conversion (5040–5110 cm^{-1}), and formation and subsequent conversion of the secondary amine (6610–6750 cm^{-1}). Arrows indicate change in absorbance as cure progresses.

time. A high concentration of primary amine indicates a molecular structure consisting mostly of low-molecular weight species. A high concentration of secondary amine indicates a mainly linear network structure. A high concentration of tertiary amine indicates a branched or crosslinked structure

The NIR absorption spectra of the Epon 828/DDS system at various levels of cure is shown in Figure 5. The assignment of the absorption bands is in general agreement with those reported in the literature.[40,48,49] A plot of the concentration of each species as a function of cure time is shown in Figure 6. NIR analysis indicates that the major chemical change during the pregelation stage of network development is the conversion of primary amine to secondary amine, which produces a linear segment. Some branching or crosslinking, however, occurs during this stage of network development as evidenced by the appearance of tertiary amine absorbance at cure times greater than 50 min. The predominant molecular architecture during the pregel phase of network development, therefore, is mostly linear oligomers with occasional branching or crosslinking. The oligomeric material increases in mass until the gel point, when it links together to form a mostly linear, infinite molecular weight network. The concentration of secondary amine continues to increase after the gel point, but reaches a maximum early in the stage of active network growth. The dominant reaction during the active stage of network growth is the conversion of secondary amine to tertiary amine—the crosslinking reaction. Essentially all of the primary amine has reacted by the midway point of the second phase of network growth meaning that most network development after this point results from intranetwork crosslinking reactions rather than the addition of unreacted monomer to the network. Tertiary amine is the dominant species during the vitrification stage of network growth. The high amount of crosslinking after vitrification restricts the ability of unreacted species to diffuse to active reaction sites.

FT-NIR analysis of epoxide concentration shows that for this curing regimen the samples do not reach a high degree of conversion prior to the onset of vitrification. An extended period of reaction time or an elevated temperature postcure step is required to drive the curing reaction to higher conversion.

Fracture pathway as an indication of nonhomogeneous crosslink distribution

Rheological, thermal, and spectroscopic characterization of the Epon 828/DDS system provides information about the development of the crosslinked network but provides no information about the distribution of crosslinks within the network. The glass transition temperature, mechanical behavior, coefficient of thermal expansion and swelling properties of thermoset epoxy systems have been shown to be dependent upon the average crosslink density of the network.[15,16,30,50] It is reasonable to expect that a nonhomogeneous distribution of crosslink density within a sample will lead to regions with different properties and present a low-energy pathway for solvent penetration or fracture propagation. This low-energy pathway provides an opportunity to use fracture surfaces as a means to investigate network heterogeneity within the Epon 828/DDS system. This can be achieved by understanding the fracture surface as the critical fracture manifold. The

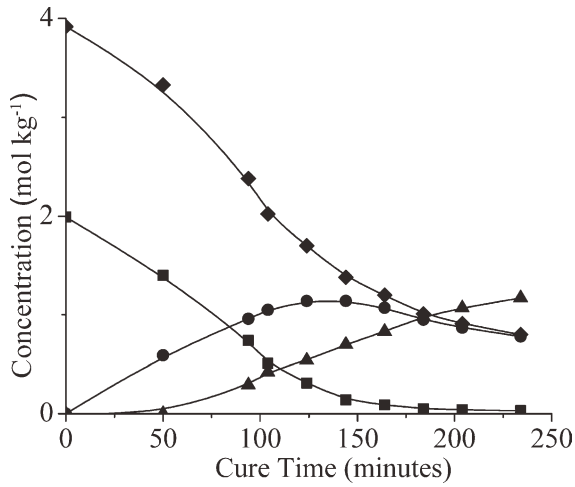

Figure 6 Concentration of epoxide (◆), primary amine (■), secondary amine (•), and tertiary amine (▲) chemical groups as a function of cure time.

critical fracture manifold is the virtual surface of the sample that follows the two-dimensional path that requires the least amount of energy to physically separate the network into two independent subnetworks.[51–53] In a similar way as the thermoplastic networks discussed previously, this fracture pathway will deviate to avoid regions with relatively higher concentrations of covalent bonds as these regions will require greater energy to propagate crack growth. The propagating crack tip will therefore deviate to preferentially travel through regions with lower crosslink density and these deviations will be preserved at the fracture surface of the sample.

The Griffith fracture criterion describes the minimum energy required to fracture a perfectly homogeneous glassy polymer below the glass transition temperature[35,54]:

$$E_f = \Delta E A$$

where E_f is the energy required to fracture the network into two subnetworks, ΔE is the surface formation energy per unit area, and A is the surface area of the fracture.[55] Since the fracture process is thermodynamically driven to produce as little new free surface area as possible, E_f is minimized when A is minimized. A is minimized when the propagating crack tip produces a planar surface, therefore perfectly planar fracture is thermodynamically favored for perfectly homogeneous materials. Inhomogeneities such as voids, inclusions, and irregular network structures such as spherulites, lamellae, and nonhomogeneous crosslink density will cause the propagating crack tip to deviate from thermodynamically preferred planar fracture.[56] The fracture pathway, therefore, results from a balance of thermodynamic and kinetic processes. The propagating crack tip is thermodynamically driven to create as little new free surface area as possible while simultaneously being kinetically driven to avoid regions that require high energy of propagation. A perfectly homogeneous network will therefore produce a perfectly planar fracture surface as the propagating crack tip finds no energy advantage in deviating from planarity. Networks with varying crosslink density will produce fracture surfaces with high deviation from planarity, as crack propagation will preferentially be driven to the lower energy, lower crosslink density regions, and these regions will be preserved at the fracture surface.

The issue of plastic deformation must be addressed before this type of analysis can be applied to the Epon 828/DDS system. The morphology of the fracture surface cannot be used to discern network structure if the observed morphology simply results from the fracture process. Samples must undergo brittle fracture with little plastic deformation. All samples were fractured at a temperature at least 25°C below the glass transition temperature. The creep characteristics of the fracture surfaces were determined by nanoindentation to understand each sample's resistance to plastic deformation at the scale of the individual nanostructures. This was done by applying a static load to the fracture surface while monitoring tip displacement over time. Figure 7 shows that, as expected, samples cured for lower amounts of time show a higher amount of plastic deformation. If the observed nodular morphology was a result of plastic deformation during the fracture process, it would be anticipated that the lowest cured samples would be most likely to exhibit the nodular morphology. The AFM images in Figure 4 show, however, that this is not the case. Alternatively, plastic deformation may be anticipated to influence the resulting fracture surface morphology by allowing the fracture surface to "recover" prior to imaging. This behavior would produce a smooth fracture surface and therefore would be likely to influence samples with a low degree of cure that were found to possess a smooth fracture surface morphology. To investigate the possibility of this behavior, a nanoscale indentation was made in the surface of a sample that would be expected to show plastic recovery. Figure 8 shows two AFM images of a sample that was cured to 20 min before the gel point. Figure 8(a) shows the indentation immediately after it was made while Figure 8(b) shows the indentation after 120 min of continuous imaging (this amount of time is far more than the interval between fracture and imaging of samples shown in Figs. 4 and 9). No recovery is observed. These investigations indicate that neither plastic deformation during the fracture process nor plastic recovery after fracture significantly affects the observed morphology of the samples.

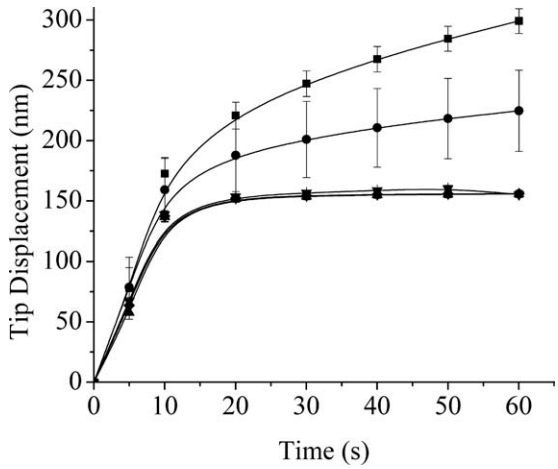

Figure 7 Tip displacement as a function of time under constant load for samples with increasing lengths of cure time.

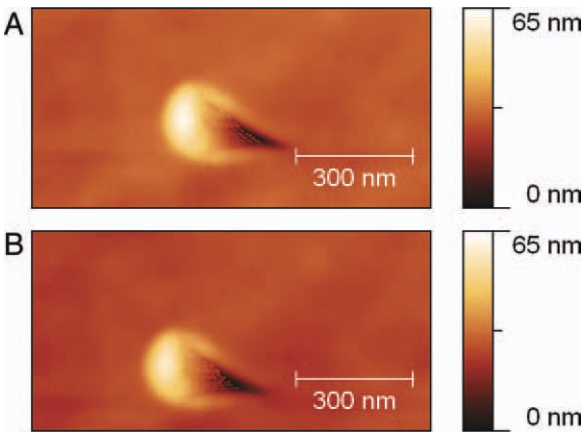

Figure 8 Topographic AFM image nanoindentation produced on surface of sample cured for 84 min (a) immediately after indentation and (b) 120 min after indentation. [Color figure can be viewed in the online issue, which is available at wileyonlinelibrary.com.]

Evolution of network connectivity in the epoxy amine system

AFM interrogation of the critical fracture manifold at increasing degrees of network development can be used in conjunction with NIR analysis of amine conversion to provide a way to understand the nanoscale distribution of crosslink density during the curing reaction of the epoxy amine system. Figure 9(A–E) shows three-dimensional projections of the topographic AFM images of the fracture surfaces. Profiles extracted from the regions marked in black are shown alongside the images. It is observed that differences in network structure influence the fracture pathway of the propagating crack tip. In Figure 10, the RMS roughness values from each image are plotted as a function of cure time, indicating increasing deviation of fracture surface from planarity with increasing curing time.

A representative AFM image of a sample fractured during the pregelation stage of network development is shown in Figure 9(A). This image shows the highly planar fracture surface indicative of a homogeneous underlying structure. The planar fracture behavior indicates that the system has a homogeneously low level of crosslinking; the critical fracture manifold does not indicate any regions with a relatively higher degree of crosslinking. The oligomeric regions have a higher amount of crosslinking than unreacted monomer, but these regions did not influence the way in which the crack tip propagated through the sample. The low number of covalent bonds in these areas may not provide a significant barrier to propagation or these regions may be so highly plasticized by unreacted monomer that they are pushed aside by the propagating crack tip.

Fracture surfaces of samples fractured during the stage of active network growth are shown in Figure 9(B–D). The development of the nanostructures during the main stage of network growth can be clearly tracked in these images. Figure 9(B) shows that the nodular nanostructures first appear at the gel point. NIR analysis shows that the sample in Figure 9(B) consists mostly of a linear network, however, an appreciable amount of tertiary amine has developed indicating the presence of some crosslinking. The concentration of tertiary amine continues to increase during the stage of active network growth as the nodular nanostructures become more regular and well-defined as seen in Figure 9(C,D). This relationship between tertiary amine concentration and morphological development indicates that the developing network consists of nodular regions of relatively higher crosslink density $\sim$ 50 nanometers in size during the main stage of network growth. Neither the number nor size of the nodular nanostructures increases appreciably during this phase of the reaction which indicates that the majority of the crosslinking reaction occurs within individual nanostructures. This result provides experimental evidence for the "gel ball" model of thermoset network development proposed by Labana.[57] In this model, a mostly linear random coil structure first develops. This structure restricts the diffusion of unreacted monomer, which then becomes trapped within the gel. As the reaction proceeds, the trapped monomer can only be added to the network within the gel ball. Eventually, enough crosslinks form within the gel to begin to restrict diffusion of unreacted monomer to active reaction sites within the gel ball and the sample becomes vitrified.

Figure 8(E) shows an image taken on the fracture surface of a vitrified sample. This image shows a significantly rougher fracture surface. NIR analysis shows that tertiary amine is the dominant amine species meaning that the majority of the network has some degree of crosslinking. The clearly defined nodules seen in Figure 8(D) have mostly disappeared. The plot of RMS roughness shows a sharp increase at the onset of vitrification. This dramatic increase in roughness indicates that the crack tip deviates strongly to follow a low energy propagation pathway. This behavior may be explained by an increase in internodular crosslinking, which prevents the crack tip from simply propagating around individual gels as it does during the main stage of network growth.

CONCLUSIONS

Identification of the molecular network structure of epoxy-amine thermosetting polymers is important for understanding structure/property relationships

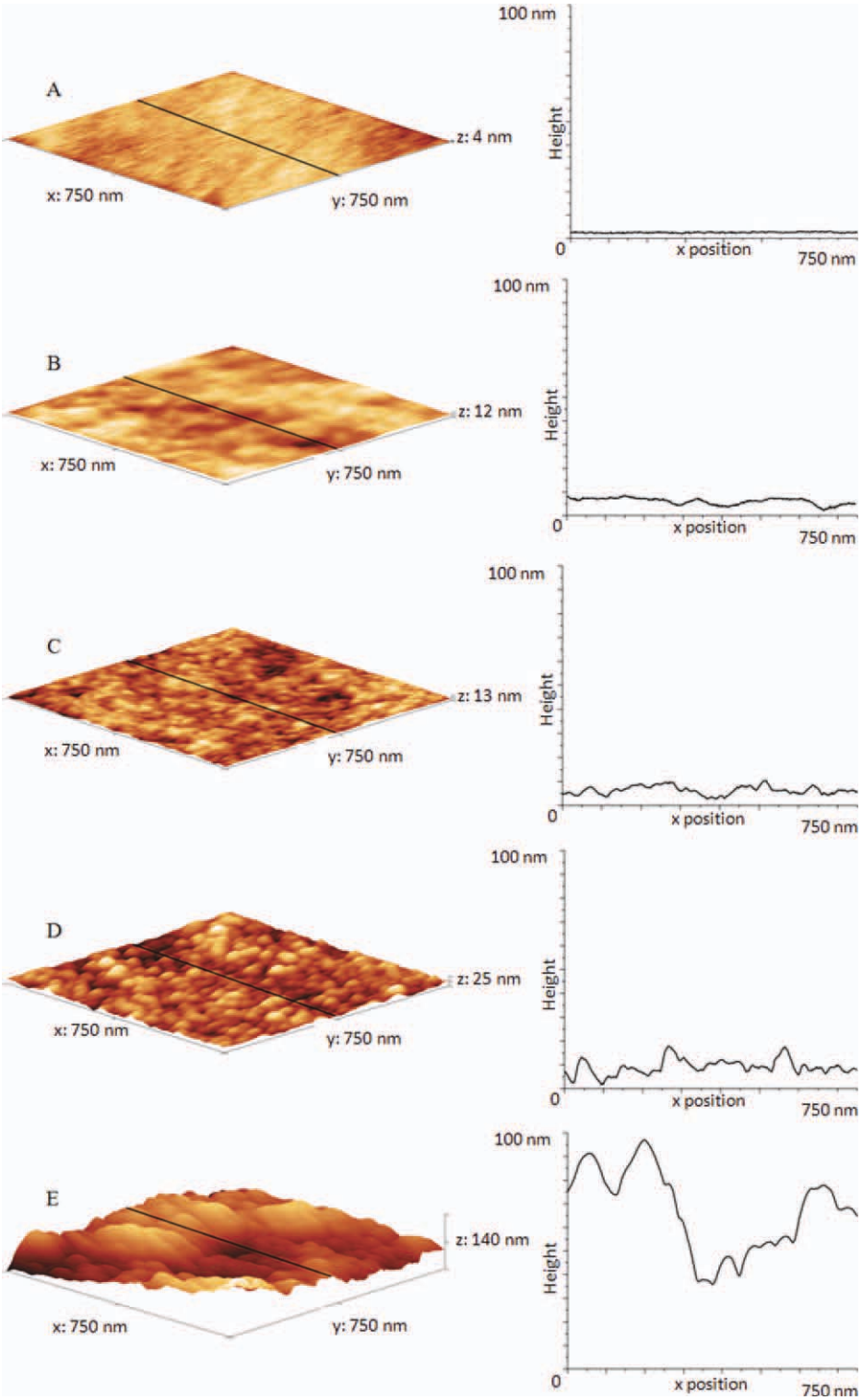

Figure 9 Topographic AFM images of the fracture surface of the epoxy-amine system at various stages of cure: (A) 84, (B) 104 (gel point), (C) 124, (D) 184, and (E) 224 min. [Color figure can be viewed in the online issue, which is available at wileyonlinelibrary.com.]

of cured systems. In this work, the fracture surface of a typical epoxy-amine system has been considered as the critical fracture manifold of the molecular network. Nanoscale morphological interrogation via AFM has been used in conjunction with data regarding amine conversion obtained by NIR spectroscopy to identify the distribution of crosslink density at increasing levels of network development. The morphology of the fracture surface was found to be different for each of the three stages of network growth

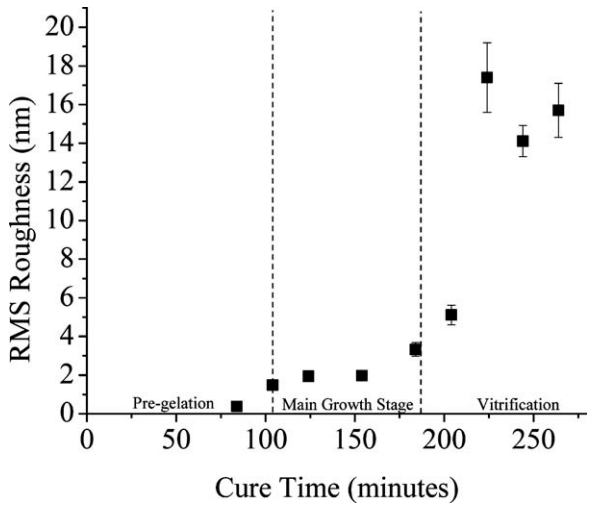

Figure 10 RMS roughness plotted as a function of cure time.

and this different morphology reflects a different underlying network structure. The distinct nodular morphology of the fracture surface indicates the epoxy-amine network undergoes a phase of nonhomogeneous crosslink density between gelation and the onset of vitrification. This morphology becomes less clear as cure progresses indicating that the distribution of crosslink density becomes more homogeneous as the overall crosslink density increases. AFM provides a useful tool for analyzing changes in the network structure of developing epoxy-amine thermoset networks and can help to identify areas of inhomogeneous network development that are important in predicting solvent permeation and mechanical properties. This type of information can be used to develop optimized curing processes and formulations as well as enhance the utilization of molecular dynamic simulations for predictive studies. Molecular dynamic simulations of these types of systems are currently the subject of further research in our laboratory.

References

1. Intelligence, A. M. World Carbon Fiber Composite Market; Acmite Market Intelligence: Ratingen, Germany, 2010, p 560.
2. Feng, J.-F.; Berger, K.; Douglas, E. P. J Mater Sci 2004, 39, 3413.
3. Choi, S.; Douglas, E. Appl Mater Interface 2010, 2, 934.
4. Haris, A.; Adachi, T.; Araki, W. Mater Sci Eng A: Struct Mater Prop Microstruct Process 2008, A496, 337.
5. Yung, K.; Zhu, B.; Yue, T.; Cie, C. J Appl Polym Sci 2010, 116, 518.
6. Ellis, B.; Found, M.; Bell, J. J Appl Polym Sci 2001, 82, 1265.
7. Lesser, A.; Crawford, E., J Appl Polym Sci 1997, 66, 387.
8. Ochi, M.; Tsuyuno, N.; Sakaga, K.; Nakanishi, Y.; Murata, Y. J Appl Polym Sci 1995, 56, 1161.
9. Madsen, P.; Foister, R., J Appl Polym Sci 1989, 37, 1931.
10. Lin, Y.; Sautereau, H.; Pascault, J. J Appl Polym Sci 1986, 32, 4595.
11. Varshney, V.; Patnaik, S.; Roy, A.; Farmer, B. Polymer 2009, 50, 3378.
12. Knox, C.; Andzelm, J.; Lenhart, J.; Browning, A.; Christensen, S. In 27th Army Science Conference; Orlando, Florida, 2010.
13. Bandyopadhyay, A.; Valavala, P.; Clancy, T.; Wise, K.; Odegard, G. Polymer 2011, 52, 2445.
14. Lin, P.-H.; Khare, R. Macromolecules 2010, 43, 6505.
15. Escher, U. Cryogenics 1995, 35, 775.
16. Chen, J. S.; Ober, C.; Poliks, M.; Zhang, Y.; Weisner, U.; Cohen, C. Polymer 2004, 45, 1939.
17. Wu, W.-L.; Hunston, D.; Yang, H.; Sten, R. Macromolecules 1988, 21, 756.
18. Levita, G.; Petris, S. D.; Marchetti, A.; Lazzeri, A. J Mater Sci 1991, 26, 2348.
19. Bicerano, J. Prediction of Polymer Properties; Marcel Dekker: New York, 1996.
20. Aspbury, P.; Wake, W. Br Polym J 1979, 11, 17.
21. Racich, J.; Koutsky, J. J Appl Polym Sci 1976, 20, 2111.
22. Errath, E. H.; Spurr, R. A. J Polym Sci 1959, 35, 391.
23. Gupta, V. B.; Drzal, L. T.; Adams, W. W.; Omlor, R. J Mater Sci 1985, 20, 3439.
24. Dusek, K.; Plestil, J.; Lednicky, F.; Lunak, S. Polymer 1978, 19, 393.
25. Gu, X.; Nguyen, T.; Ho, D.; Oudina, M.; Martin, D.; Kidah, B.; Jasmin, J.; Rezig, A.; Sung, L.; Byrd, E.; Jean, Y. C.; Martin, J. J Coat Technol Res 2005, 2, 547.
26. Gu, X.; Sung, D.; van Landingham, M.; Nguyen, T. Proc Mater Res Soc 2002, 710, DD109.1.
27. Nguyen, T.; Gu, X.; van Landingham, M.; Giraud, M.; Dutruc-Rosset, R.; Ryntz, R.; Nguyen, D. In 24th Annual Meeting of the Adhesion Society; Williamsburg, VA, 2001; p 68.
28. van Landingham, M.; Eduljee, R.; Gillespie, W. J Appl Polym Sci 1998, 71, 699.
29. Morgan, R.; O'Neal, J. J Mater Sci 1977, 12, 1966.
30. Kim, H.; Kent, M.; McNamara, W.; Ivkov, R.; Satija, S.; Majewski, J. Macromolecules 1999, 32, 7932.
31. Mijovic, J.; Tsay, L. Polymer 1980, 22, 902.
32. Kenyon, A. S.; Nielsen, L. E. J Macromol Sci: Chem 1969, A3, 275.
33. Matyi, R.; Uhlmann, D. J Polym Sci: Polym Phys Ed 1980, 18, 1053.
34. Gogolewski, S. Polymer 1977, 18, 647.
35. Kausch, H. H. Polymer Fracture; Springer-Verlag: Berlin, 1978.
36. The American Society of Mechanical Engineers. ASME, New York, NY, 1995.
37. Franck, A. APN007; TA Instruments: New Castle, DE, p 8.
38. Chambon, F.; Winter, H. J Rheol 1987, 31, 683.
39. Winter, H.; Chambon, F. J Rheol 1986, 30, 367.
40. Min, B. G.; Stachurski, Z. H.; Hodgkin, J. H.; Heath, G. R. Polymer 1993, 34, 3620.
41. Riccardi, C.; Williams, R. J Appl Polym Sci 1986, 32, 3445.
42. Pharr, G.; Oliver, W.; Brotzen, F. J Mater Res 1992, 7, 613.
43. Kim, D. H.; Kim, S. C. Polym Bull 1987, 18, 533.
44. Assche, G. V.; Hemelrijck, A. V.; Rahier, H.; Mele, B. V. Thermochim Acta 1995, 268, 121.
45. Halley, P.; George, G. Chemorheology of Polymers; Cambridge University Press: Cambridge, 2009.
46. Magonov, S.; Elings, V.; Whangbo, M. Surf Sci 1997, 375, L385.
47. McLean, R.; Sauer, B. Macromolecules 1997, 30, 8314.
48. Xu, L.; Fu, J. H.; Schlup, J. R. J Am Chem Soc 1994, 116, 2821.
49. George, G. A.; Cole-Clarke, P. A.; John, N. A. S.; Friend, G. J. J Appl Polym Sci 1991, 42, 643.
50. Urbaczewski-Espuche, E.; Galy, J.; Gerard, J.-F.; Pascault, J.-P.; Sautereau, H. Polym Eng Sci 1991, 31, 1572.
51. Holm, E.; Duxbury, P. Script Mater 2006, 54, 1035.
52. Holm, H.; Meinke, H.; McGarrity, E.; Duxbury, P., Mater Sci Forum 2004, 467–470, 1039.
53. Holm, E. J Am Ceram Soc 1998, 81, 455.
54. Griffith, A. A. Philos Trans R Soc London A 1921, 221, 35.
55. Holm, E. A.; McGovney, G.; Microscale Modeling and Simulation; Sandia National Laboratories: Albuquerque, NM, 2000, 42.
56. Holm, E.; McGovney, G.; Minimum Surface Formation Energy for Three-Dimensional Intergranular Fracture; Sandia National Laboratories; Albuquerque, NM, 1999.
57. Labana, S.; Newman, S.; Chompff, A. Polym Networks: Structural and Mechanical Properties; Plenum: New York, 1971.